AGU PUBLICATIONS

Geophysical Research Letters

RESEARCH LETTER
10.1002/2017GL073342

Key Points:
- Convective scales increase systematically after precipitation onset
- The increase is only weakly sensitive to temperature forcing and initial temperature profiles
- Convective precipitation extremes may be caused by an earlier precipitation onset

Correspondence to:
J. O. Haerter,
haerter@nbi.dk

Citation:
Haerter, J. O., P. Berg, and C. Moseley (2017), Precipitation onset as the temporal reference in convective self-organization, *Geophys. Res. Lett.*, *44*, 6450–6459, doi:10.1002/2017GL073342.

Received 17 MAR 2017
Accepted 18 MAY 2017
Accepted article online 22 MAY 2017
Published online 28 JUN 2017

Precipitation onset as the temporal reference in convective self-organization

Jan O. Haerter[1], Peter Berg[2], and Christopher Moseley[3]

[1]Niels Bohr Institute, University of Copenhagen, Copenhagen, Denmark, [2]Swedish Meteorological and Hydrological Institute, Norrköping, Sweden, [3]Max Planck Institute for Meteorology, Hamburg, Germany

Abstract In a dry convective boundary layer, convective patterns of typical scales spontaneously develop, qualitatively similar to those in a fluid which is placed between two horizontal plates and sufficiently heated from below. As soon as precipitating cumulus clouds form, this pattern is disturbed and a transition to a different state occurs. Here we use idealized large-eddy simulations to explore how the horizontal scale of convection is modified during this transition in the course of a diurnal cycle. Before onset of precipitation, cells with relatively constant diameter self-organize, with diameters roughly on the scale of the atmospheric boundary layer height. We find that the onset of precipitation then signals an approximately linear increase in horizontal scale with time. For our transient simulations, this scale increase progresses at a speed which is relatively insensitive to modifications in mean surface temperature, modifications in the rate at which surface temperature changes, or the initial lapse rate. When exploring the strength of the spatial correlations, we find that precipitation onset causes a sudden disruption of order and a subsequent decline of organization—until precipitation eventually ceases. We discuss possible implications for the development of extreme precipitation events.

Plain Language Summary When a fluid is placed between two horizontal plates and the lower plate is sufficiently heated, the fluid undergoes a dynamical motion where convective cells of typical diameter are formed. Within the cells, the fluid rises and sinks in a systematic way. The air of the atmosphere is similar to such a fluid system; it, however, contains moisture which can produce clouds and precipitation. When clouds form through condensation, this can be seen as a heating process, leading to a disruption of the patterns initially formed. We show that after onset of precipitation the typical diameter of structures within the atmosphere systematically increases throughout the course of the day. The increase is found to be rather independent of how much the surface is heated or which configuration of temperature is used to initialize the atmosphere in the morning. Our results show that the onset of precipitation is a characteristic time which can be used to compare very different numerical experiments. For the real-world atmosphere our results have important implications regarding extreme rainfall. Such extreme rainfall has been found to react strongly to changes in surface temperature. Our results make a step toward explaining how this can be the case.

1. Introduction

For a fluid between two infinite horizontal plates and a sufficient temperature difference between these two boundaries, classical Rayleigh-Bénard convection predicts that the fluid will undergo a transition from uniform vertical heat transport to the formation of convective cells [*Rayleigh*, 1916; *Bénard*, 1901]. In the atmosphere, comparable, albeit generally much less idealized, circumstances exist, when the surface is approximately planar and the atmospheric boundary layer is capped by a stable inversion layer [*Atkinson and Zhang*, 1996]. Despite differences, e.g., larger Rayleigh numbers in the atmosphere [*Emanuel*, 1994], relatively long-lived convective patterns are nonetheless observed, such as open and closed cell structures in the marine stratocumulus regime [*Agee et al.*, 1973].

Earth's atmosphere crucially differs from one-phase lab conditions, as atmospheric air contains various phases of water, which enable cloud formation and precipitation. For marine stratocumulus clouds it was shown that even weak precipitation can alter the patterns of clouds, induce structural transitions, and give rise to oscillations [*Feingold et al.*, 2010; *Koren and Feingold*, 2011]. Indeed, the persistence of convective updrafts is counteracted by the release of latent heat aloft during cloud formation, redistribution of moisture

during a precipitation event, and possible rain evaporation near the surface. The latter can induce cooling and the formation of cold pools [*Tompkins*, 2001; *Engerer et al.*, 2008; *Böing et al.*, 2012; *Schlemmer and Hohenegger*, 2014].

Furthermore, observations of precipitation from convective clouds have recently drawn attention, as they point to previously unexpected temperature sensitivity of convective extremes over land [*Lenderink and van Meijgaard*, 2008; *Berg et al.*, 2013; *Moseley et al.*, 2013; *Molnar et al.*, 2015]: at higher surface temperatures and small spatiotemporal scales, extreme precipitation can strengthen at rates beyond the Clausius-Clapeyron rate (∼7%/K). The "null hypothesis," where thermodynamic limits alone cap increases of intensity, is thereby likely ruled out, and dynamical effects have been brought into discussion.

Global and regional climate models serve as the principal tool for projecting future changes in precipitation. With relatively coarse scales (∼10–100 km horizontally) their simulations mostly rely on parameterizations of convective cloud processes. Such parameterizations are often founded on the simplifying radiative convective equilibrium (RCE) assumption for convection. RCE states that when the atmosphere adjusts relatively quickly to changes in boundary conditions, convection can be seen to occur in a stepwise equilibrium dynamics: at each step, the incoming radiation should equal the outgoing and convective cloud should adjust rapidly.

More recent studies, however, show that such equilibrium is not generally a sufficient approximation for tropical [*Neelin et al.*, 2008] or midlatitude precipitating convection [*Moseley et al.*, 2016]. Large-eddy simulations (LES) indicate that the response of convective cloud to changing boundary conditions is substantially delayed and—as clouds grow larger and become more widely spaced throughout the day—precipitation continues to intensify although the heating or total convective available potential energy (CAPE) are already on the decline [*Moseley et al.*, 2016]. Further, whereas classical models often assume a statistical ensemble of noninteracting clouds, the results imply that observed intensifications of precipitation must be understood by taking into account the interaction between clouds.

We here analyze the diurnal evolution of the convective correlation structure over an idealized land surface for typical midlatitude summer conditions. The simulations comprise a smoothly varying surface temperature forcing, which drives an initially stable boundary layer to transition to free convection, thereby setting off significant precipitation. We contrast a suite of numerical experiments, which differ either by different surface temperature forcing or by different initial conditions, and show where they differ and how they can nonetheless be compared on an equal footing.

After a qualitative discussion of the convective moisture dynamics, we quantify the spatial correlation structure. We then determine the typical horizontal scale of convective cells and compare various simulations, finding that in all simulations, precipitation sets off a roughly linear scale increase. When varying surface temperature forcing or the initial vertical temperature profile, the overall amount of precipitation changes strongly. However, the rate of scale increase is affected relatively little. The results therefore suggest that horizontal convective scales may self-organize in a way that is only weakly sensitive to the details of heating or temporal boundary conditions—as long as precipitation is allowed to unfold and impact on organization. We close by a discussion of possible implications of our work.

2. Materials and Methods

2.1. Simulation Setup

The simulation setup is similar to that in *Moseley et al.* [2016], and we repeat its description here for clarity. Idealized diurnal cycles over a land surface are simulated using the University of California, Los Angeles (UCLA) LES model [*Stevens et al.*, 2005]. The LES uses a delta four-stream radiation scheme [*Pincus and Stevens*, 2009] and a two-moment cloud microphysics scheme [*Seifert and Beheng*, 2006]. Subgrid-scale turbulence is parametrized after *Smagorinsky* [1963]. In both horizontal dimensions, the resolution is 200 m and double-periodic boundary conditions are applied. The surface is flat and homogeneous; i.e., the system is translationally invariant in both horizontal directions. We use 75 vertical levels with spacings of 100 m below 1 km stretching to 200 m around 6 km and 400 m in the upper layers. The model top is located at 16.5 km with a sponge layer above 12.3 km.

2.2. Initial and Boundary Conditions

The basic simulation is set up to simulate a diurnal cycle with convective activity evolving throughout the day. We therefore base the initial vertical temperature and humidity profiles on typical radio soundings taken

at the super site Lindenberg, Germany, during the two summers of 2007–2008. Only potentially convective days, defined as days with a CAPE value larger than 1000 J kg^{-1} at 12 UTC, are retained. The idealized temperature profile is obtained by prescribing a temperature lapse rate of 6.6 K km^{-1} below 11 km and 3 K km^{-1} above 11 km starting from a surface temperature of 21°C. The profile of relative humidity is idealized as follows: Relative humidity linearly increases by 7.5% km^{-1} below 2 km and decreases by 12.5% km^{-1} between 2 and 4 km, by 2% km^{-1} between 4 and 10 km, and by 12% km^{-1} higher up. Surface relative humidity is set to 65%. Knowing temperature and relative humidity, the idealized profile of specific humidity is obtained. Background wind is set to 0. The initial profiles of temperature and humidity are then set equal for all horizontal positions within the model domain. However, in order to break the resulting perfect translational symmetry in the horizontal, weak random noise is added to the initial state of the atmosphere.

At the surface, the sensible and latent heat fluxes are computed interactively by the model using Monin-Obukhov similarity theory and a prescribed surface temperature T_{surf}. The diurnal cycle of T_{surf}, measured at Lindenberg and averaged over the previously defined convective days, is approximated by the following relationship: $T_{surf} = T_0 + T_A \sin((2t/t_d - 1/2)\pi)$ with t time and $t_d = 24$ h. The daily mean temperature T_0 was varied for the different simulations, but its amplitude $T_A = 10$ K remained fixed. To account for the fact that evaporation does not occur at its potential rate at Lindenberg, the saturation specific humidity is reduced by 30%. The chosen values give a daily averaged sensible and latent heat flux of 21.8 and 67.1 W m^{-2} in CTR versus 13.8 and 71.9 W m^{-2} at Lindenberg. As we start from zero background wind, the surface fluxes are 0 during night, whereas the observed latent heat flux amounts to 30 W m^{-2}. During daytime, both fluxes are overestimated in CTR as compared to the observations, but the Bowen ratio remains similar. The Bowen ratio amounts to 0.33 in CTR and 0.32 in the observations at 12 local standard time. All simulations are initialized at 0 UTC and run over one diurnal cycle, which is triggered by solar insolation at the latitude of Lindenberg (52°N) in midsummer.

2.3. Definitions

We define the *two-point correlation function* C for a scalar observable $q(x, y, t)$ at a given time t, and horizontal position (x, y). $q(x, y, t)$ is not a function of the vertical coordinate; it may hence be a vertically averaged quantity. $C(\delta_x, \delta_y, t) \sim \int_x \int_y \mathrm{d}x\mathrm{d}y \;\; q(x, y, t)q(x + \delta_x, y + \delta_y, t)$ compares q at two horizontal positions that are displaced by the vector (δ_x, δ_y) at the same time t. Due to the uniformity and symmetry of the model domain, we assume symmetry regarding the two horizontal coordinates. We compute all correlations $C(\delta_x, 0, t)$ and $C(0, \delta_y, t)$ and then average over all values where $|\delta_x| = |\delta_y|$, yielding an average correlation function $C(|\delta|, t)$ for each magnitude of δ, where $\delta \equiv |\delta_x|$ or $\delta \equiv |\delta_y|$, respectively. For technical reasons we only compute correlations in x and y directions and not, e.g., along the diagonal. The resulting correlation function $C(|\delta|, t)$ is hence dependent on spatial distance $|\delta|$ as well as the time step t. To obtain a clearer signal, we coarse grain time by averaging over several (n) values of t; i.e., several time steps are aggregated. With the model output interval $\Delta_t = 5$ min, the temporal average of $\tilde{C}(|\delta|, t)$ for n time steps is hence defined as $\tilde{C}(|\delta|, t) \equiv \sum_{m=0}^{m=n-1} C(|\delta|, t + m \cdot \Delta_t)/n$. For simpler notation, in the text we use the symbol C instead of $\tilde{C}$.

Liquid water path (LWP) is defined as the total amount of liquid water, excluding rain water, contained in an atmospheric column. We use it as a proxy for "cloud amount" within each atmospheric column.

Precipitation yield and *intensity* are defined as the total instantaneous rate of precipitation in the model domain divided by domain area, respectively the domain area where rain occurs (theshold: 0.1 mm h^{-1}).

2.4. Numerical Experiments

We employ the results of several numerical experiments: A "control" simulation (termed CTR) was set up such that it provides significant, but not excessive, convective precipitation. Average surface temperature set to $T_0 = 23$°C was found appropriate. We performed additional simulations where temperature was increased by 1 K (termed P1K), 2 K (P2K) and 4 K (P4K). We performed a simulation termed LAPSE, where average surface temperature was again increased to $T_0 = 25$°C, but the initial vertical temperature profile was additionally increased by 2 K in the lowest model level. This profile then, however, decreased more rapidly with height to approximately match that of CTR above 5000 m, thus increasing the lapse rate. Relative humidity was preserved to the values of CTR, so that an overall larger value of CAPE resulted for LAPSE. All these simulations were carried out on a domain of approximately 200 km × 200 km. *Moseley et al.* [2016] introduced the "longer day" (LD) simulation to allow convection ample time to develop while otherwise maintaining the boundary conditions of CTR. LD has identical boundary conditions to CTR but an overall temporal stretch of the model day by a factor of 2, on a smaller domain (approximately 100 km × 100 km). The stretch of time

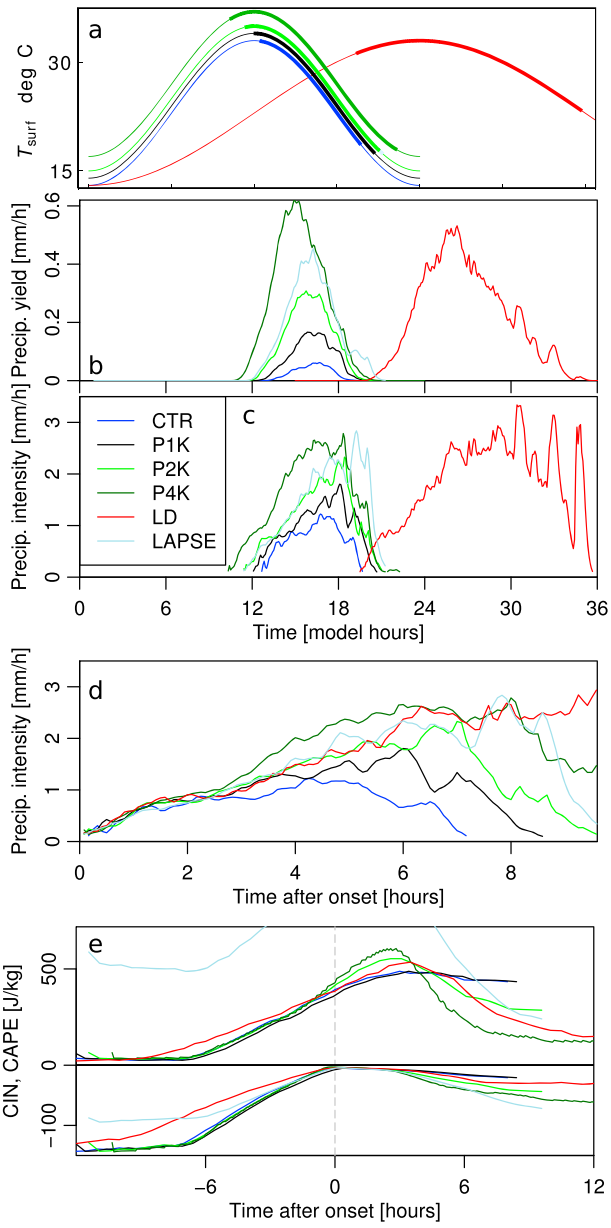

Figure 1. Diurnal cycles of various quantities. (a) Prescribed surface temperature versus model hours. Different curves correspond to the simulations CTR, P1K, P2K, P4K, LD, and LAPSE as shown in the legend in Figure 1c. Bold curve segments highlight the times when precipitation occurred in the simulations (the curve of LAPSE coincides with that of CTR except for an earlier onset of precipitation). (b) Precipitation yield, i.e., total areal precipitation intensity. (c) Precipitation intensity, i.e., average precipitation intensity for areas with rain. (d) As in Figure 1c but with time shifted to be relative to precipitation onset. (e) CAPE (top) and CIN (bottom) relative to precipitation onset. Note the different vertical scales for CAPE and CIN. Legend shown in Figure 1c applies equally to all panels.

resulted in a model day of $t_d = 48$ h, where boundary conditions, i.e., the surface heating as well as solar irradiation, varied at half the rate but conditions were otherwise identical to CTR. In all numerical experiments, the 3-D fields of prognostic variables are output instantaneously at a $\Delta_t \equiv 5$ min interval.

3. Results

We performed a control simulation (CTR) to mimic a typical convectively unstable atmosphere over a midlatitude land surface, where average surface temperature was set to 23°C (Details: section 2.4). At such temperatures, rain predominantly results from convective precipitation in this region. The remaining simulations were carried out to explore three types of responses to changed boundary conditions: First, by increasing surface temperature forcing (simulations P1K, P2K, and P4K), we address the dynamical response to varying surface temperature. Second, in changing the vertical profiles of temperature and humidity (LAPSE), we further destabilize the atmosphere by allowing for greater buoyancy. Greater buoyancy might accelerate updrafts and lead to faster organization of the cloud field—a feature not directly visible when only modifying surface temperature. Third, we test against a simulation, where only the time dependence, but not the average value of surface temperature and solar irradiation, was modified (LD). This simulation tests the memory of the atmosphere and its latency in reacting to changes in boundary conditions. One might wonder whether a slower rate of boundary condition changes would also lead to similarly slow organization of the atmosphere throughout the model day.

3.1. Precipitation Onset as Temporal Reference

For comparison of all five simulations we highlight the period within which precipitation occurs (bold segments in Figure 1a), indicating that onset and termination of precipitation vary from simulation to simulation. For the CTR, P1K, P2K, and P4K experiments, which only differ in the offset in surface temperature, the duration of precipitation increases systematically with higher temperature (earlier onset and later termination). In LD, which shares average surface temperature with CTR, precipitation is initiated at the overall lowest temperature but ceases at a higher temperature than in all other simulations. LAPSE gives similar initiation and termination as P2K. These differences can be explained, when considering that the atmosphere does not adjust instantaneously

to surface temperature changes. Higher surface temperature then raises the temperature in the lowest atmospheric levels relative to the ones farther aloft, thereby inducing a stronger convective instability relative to lower surface temperatures.

The simulations are also markedly different in the magnitude of precipitation yield (Figure 1b) and intensity (Figure 1c). Both increase with elevated temperature (e.g., P1K, P2K, and P4K versus CTR) or overall duration of the model day (LD). LAPSE, where the larger lapse rate increases the convective instability, also gives elevated precipitation rates. As noted previously [*Moseley et al.*, 2016], it is important to remember that largest intensities tend to occur later in the day, when overall yield is already on the decline (compare Figures 1b and 1c).

We now aim to compare all these simulations by a common reference. While precipitation yield clearly differs between simulations, it has recently been shown that LES-simulated precipitation intensity depends on the state of convective organization [*Moseley et al.*, 2016]. Consider, therefore, the evolution of precipitation intensity relative to the *onset* of precipitation (Figure 1d). Indeed, all simulations give very similar intensities up to approximately 2 h after precipitation first sets in. After this time simulations with longer precipitation durations reach higher intensities. A common feature of all simulations is that the convective inhibition (CIN) is reduced to nearly 0 at the onset of precipitation (Figure 1e). As we now test, the organization of the atmosphere is very similar in all simulations, when precipitation is first triggered and during the subsequent temporal development.

3.2. Spatial Patterns

We have, so far, only discussed spatial mean quantities as a function of time. A more complete characterization of the atmospheric state throughout the day requires some measure of the spatial structure. A quantity that links Rayleigh-Bénard convection to precipitation is the horizontal moisture convergence field, i.e., the net rate of water vapor and cloud water advected into an atmospheric column, $C_q \equiv -\int_{z_0}^{z_1} \nabla \cdot (q\vec{v})\rho dz$, where q is the moisture mixing ratio, $\vec{v}$ is the wind field, and ρ is the density of air.

Figure 2 qualitatively shows low-level ($z_0 = 0, z_1 = 2000$ m) horizontal moisture convergence for various stages of convective development throughout the day. Moisture convergence is an important quantity in determining locations of likely occurrence of free convection, as higher values of moisture can increase buoyancy and reduce convective inhibition. The time of reference was again chosen to be precipitation onset (denoted as t_0), and times before and after the onset are displayed. Before t_0, the pattern consists of thin filaments of convergence and patches of divergence, both of relatively moderate magnitude. At t_0, small regions of extreme convergence appear, which are soon thereafter followed by precipitation and subsequent divergence of moisture. What is apparent when comparing the temporal evolution is that, over time, patterns become more coarse and fluxes more intense. When inspecting the patterns from simulation to simulation, it is remarkable that the patterns at similar times relative to precipitation onset are qualitatively similar for the different simulations, with structures showing similar size and shape. The similarities between the different experiments are remarkable, given that all simulations have significantly different boundary conditions and different times of day are compared. About 2 h after t_0, differences in the magnitude of fluxes start to become apparent, which we will more quantitatively assess below.

3.3. Quantifying Spatial Scales

We now study the two-point correlation function of convergence $C(|\delta|, t)$ at a given time t (Details: section 2.3). Mirroring our discussion of Figure 2, before the onset of precipitation all four simulations show pronounced anticorrelations at small spatial scales (Figure 3), with typical minima of $C(|\delta|, t)$ at $|\delta| \sim 1$ km. Considering that the patterns in Figure 2 are characterized by large patches of divergence and only narrow segments of convergence, it is fortunate that the simple measure $C(|\delta|, t)$ nonetheless shows a sufficiently clear signal, even at later stages of the day when patterns become more strongly perturbed.

Within the resolution of the model, the scale $|\delta|$ remains essentially unchanged until the onset of precipitation (Figure 3). Such constancy could be explained by the presence of relatively stable Rayleigh-Bénard-like convection at this stage, where precipitation is not present and the system cannot be perturbed by the rapid redistribution of moisture and heat through rainfall and its evaporation near the surface. In all simulations, the situation changes markedly after precipitation sets in (red curves in Figure 3). Scales now systematically increase, and 6 h after onset of precipitation, anticorrelated regions are approximately 10 km apart. Hence, correlations between updrafts are now on the order of 20 km. Clouds tend to be larger and precipitation

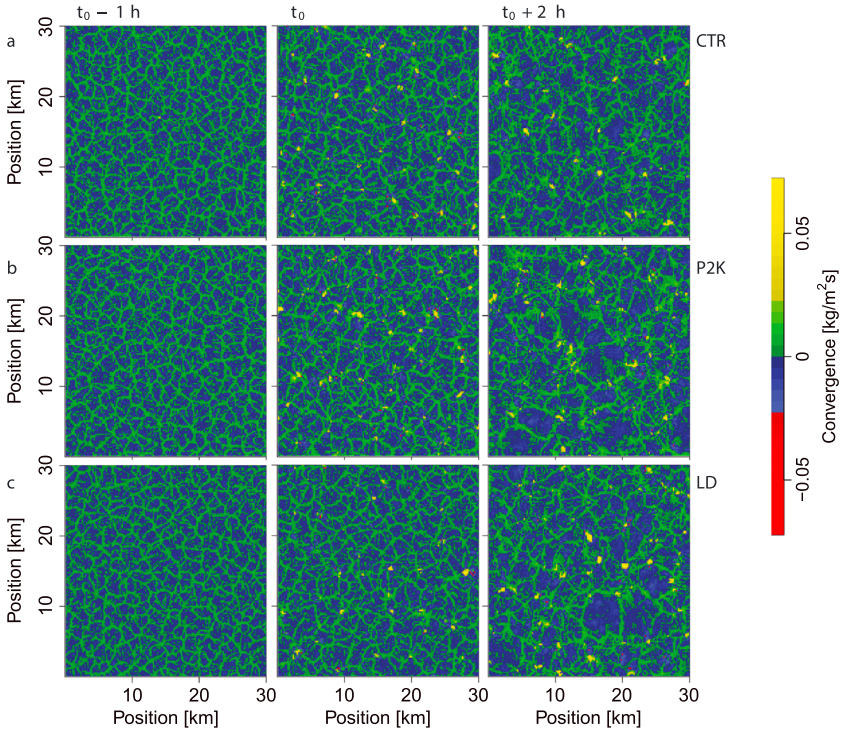

Figure 2. Qualitative stages of convective self-organization. Top view of vertically integrated moisture convergence below 2000 m at various stages of convective development; areas of extreme moisture convergence are shown in yellow. Panels from left to right correspond to the times 1 h before onset of precipitation ($t_0 - 1$ h), at the onset (t_0), and 2 h after the onset ($t_0 + 2$ h), respectively. (a) CTR, (b) P2K, and (c) LD. P1K, P4K, and LAPSE gave qualitatively similar patterns and are therefore not shown.

more intense. Qualitatively similar results are obtained for simulations with large-scale advective forcing for the transverse direction, however with larger rates of scale increase.

To focus more explicitly on the most typical horizontal scale, we extract from Figure 3 the value of $|\delta|$ where the minimum in correlation occurs (termed δ^*), as well as the depth of the anticorrelation, i.e., the minimum value of each curve. The *organization scale* $2\delta^*$, i.e., the distance between similar convergence structures, is

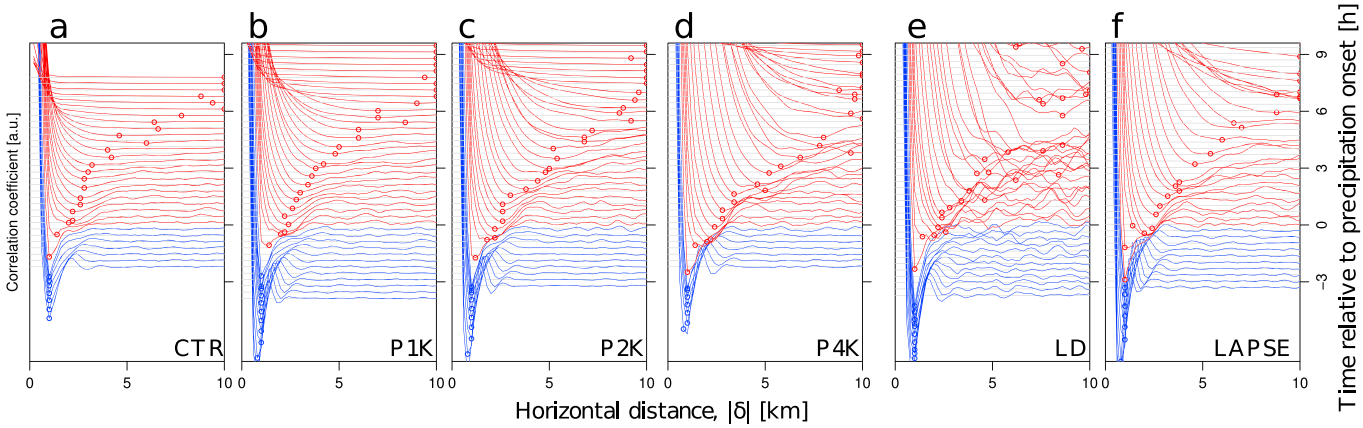

Figure 3. Spatial moisture convergence correlations. Correlation functions in arbitrary units computed by evaluating the two-point correlation $C(|\delta|, t)$ of low-level moisture convergence. Blue (red) curves show the correlation function for a given time during the simulation before (after) the onset of precipitation. Thin gray lines indicate the respective value of neutral correlation for each curve, which were shifted vertically for ease of presentation. The right vertical axis indicates the respective time when each correlation function was measured. Symbols on curves indicate δ^*, i.e., the value of $|\delta|$ with maximal anticorrelation. Note the near constant δ^* before onset of precipitation and the approximately steady increase of δ^* after the onset. (a–f) The simulations as marked in the lower right corner of each panel.

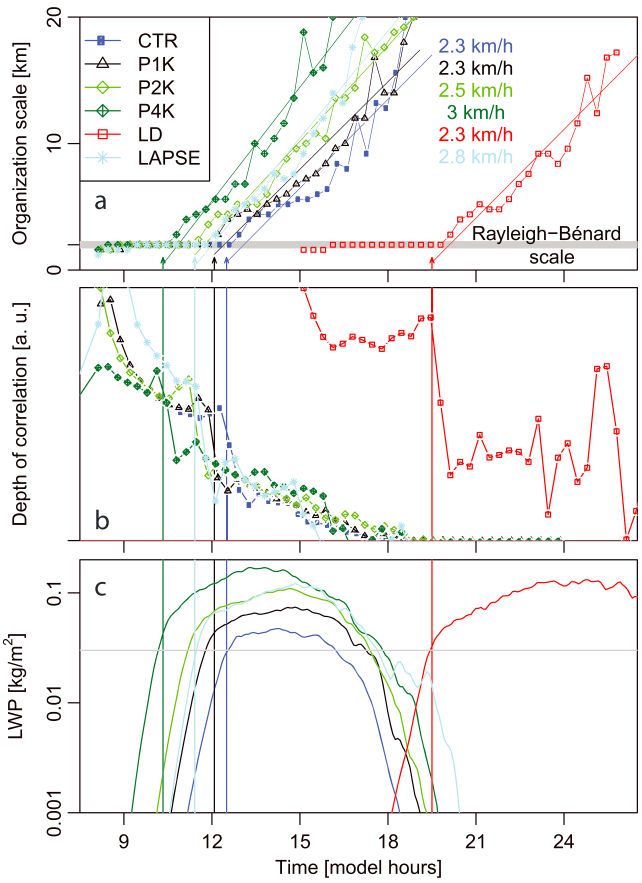

Figure 4. Time dependence of correlations and liquid water. (a) Organization scale versus time for all simulations as shown in legend. Note the approximate constancy of organizational scale up to the time t_0 of precipitation onset (colored arrows) and the approximately linear increase of scale after precipitation onset ($t > t_0$). Thin colored lines show fits to the functions after onset of precipitation. Numbers indicate rates of increase in scale for the different simulations. (b) Depth of correlations (arbitrary units, as only the relative change is of interest). Note the general decay over time and the more abrupt decay shortly after onset of precipitation. (c) Cloud water (measured as LWP) as a function of time. Note the logarithmic vertical scale. The gray horizontal line is a guide to the eye, marking the value of LWP where in both CTR and LD precipitation sets on. Onset of precipitation marks a transition from a steep, approximately exponential, increase in cloud water to a saturation regime.

shown as a function of time in Figure 4a. Its initial value is very similar and constant in all simulations ($2\delta^* \approx 2$ km). As precipitation sets in ($t = t_0$), scales systematically increase for all simulations. To extract the rate of scale increase, we fit linear functions to the curves after the onset ($t > t_0$), yielding the rate of increase as the slope of these lines. Despite substantial noise, these rates turn out to be approximately similar in the four simulations ($d|\delta|/dt \approx 2.5$ km/h), hinting at some process other than the forcing boundary conditions or the initial temperature profile, that might determine the scale increase. P2K and P4K indicate a consistent small increase of $d|\delta|/dt$ with increases in surface temperature; however, the differences are within the margin of error of the straight line fit.

When sensitivity of results to large-scale forcing is considered, results are qualitatively similar. We used simulations with horizontal wind increasing linearly from 0 at the surface to 10 ms^{-1} at 10 km height and constant 10 ms^{-1} above 10 km. Again, the spatial scale remains constant before precipitation onset and there is a steady scale increase after the time of onset. The rate of scale increase is, however, found to be approximately doubled with the forcing ($d|\delta|/dt \approx 5$ km/h), a speedup that might be attributable to the effective advection speed of rain fields (≈ 3 ms^{-1}) yielding effectively faster progression of interactions between clouds.

3.4. Decay of Correlation Signal

To quantify how pronounced the correlations are in different simulations, we analyze the depth of correlations (Figure 4b), i.e., the magnitude of the curves in Figure 2 when they reach their respective minima. In contrast to the organizational scale, which changes little before the onset of precipitation, the depth of correlation does decrease already before precipitation onset (curve segments before vertical colored lines). Such a decrease of correlation could in part be explained by increasing departure from classical Rayleigh-Bénard convection and relatively stationary convective cells, when vertical temperature differences grow due to surface temperature increase. Notably, for LD, correlations are stronger and vary less in time. We speculate that at any given temperature the system might tend to approach a more stationary pattern, which it then needs to reorganize when the temperature boundary conditions are changed.

The jump at precipitation onset could be understood better when examining cloud water, i.e., the liquid water path (LWP) (Figure 4c). Before precipitation onset, LWP increases approximately exponentially. Near the onset, LWP transitions to a plateau-like regime, where smaller changes in LWP occur. This plateau is indicative of a saturation process, where new clouds continue to be formed but a fraction of the existing ones dissipates

through ongoing precipitation. The level of saturation increases systematically with increasing surface temperature forcing; however, also when longer buildup of moisture is allowed as in LD, large values of LWP can be obtained.

The disruption of correlations by precipitation can be understood physically: through precipitation, strong and abrupt redistribution of latent heat occurs between the boundary layer and the free troposphere. In the boundary layer, melting and evaporation of precipitation lead to additional cooling and formation of cold pools [*Engerer et al.*, 2008; *Schlemmer and Hohenegger*, 2014, 2015; *Torri et al.*, 2015]. The effect of cold pool formation is to counteract the initiation of new convective cells, whereby updrafts are converted to downdrafts and birth of new convective cells can occur nearby, in locations of previous downdrafts [*Tompkins*, 2001; *Moseley et al.*, 2016]. When surface temperature forcing is reduced in the evening, precipitation generally ceases and the atmosphere gradually relaxes.

4. Discussion

Convective self-organization is a notoriously challenging topic, yet it may hold the key to understanding how extreme convective precipitation forms and how the cloud field is structured also at larger scales such as in mesoscale convective systems or the Madden-Julian Oscillation [*Moncrieff*, 2010]. Conceptually, we view the cloud ensemble as an interacting system. Initial moisture convergence can set off precipitating convection, which eventually induces downdrafts by condensation heating aloft and evaporative cooling near the surface—in turn reducing CAPE and increasing CIN locally. As a result, further precipitation in a given location is inhibited, but the divergent outflow from the decaying event (cold pool) can lead to convergence elsewhere, especially in locations where cold pools collide. Convective precipitation events resulting from such collisions are often more intense than those without collisions, and colliding events late in the day are stronger and larger than those at earlier times [*Moseley et al.*, 2016].

The qualitative picture capturing this dynamics is that of a patchwork of four generic states: "excitable" states with low CIN and high CAPE, where precipitation events could be set off by small perturbations; "excited" states, where CAPE becomes depleted and downdrafts are created; "recovering" states, where precipitation has recently occurred and further precipitation is inhibited by depleted CAPE and elevated CIN; and "activated" states, where cold pool collisions can trigger strong convective precipitation. The interplay of these four states over time will result in a two-dimensional organization of configurations. We propose that this model should be explored in terms of a dynamical simulation.

5. Conclusion

We have addressed the transient self-organization of precipitating convection in an idealized atmosphere under plausible diurnal surface temperature forcing. Our work shows how the cloud system organizes from within, and typical scales emerge. In the simulation setup, wind shear, surface inhomogeneity, and the Coriolis force were removed, yielding a translationally invariant system. This work explores how the correlation structure of the atmosphere evolves, taking precipitation onset as the "natural" reference time. Indeed, within this approach, several aspects of convective evolution become more "universal," meaning that even within differing temporal boundary conditions, similar characteristics can be obtained: precipitation intensity evolves similarly after precipitation sets in and even hours after the onset intensities are still comparable for all our numerical experiments. Spatial patterns, measured in terms of low-level moisture convergence, are visually similar.

Quantification in terms of a two-point correlation function indeed confirms that horizontal scales increase at generic rates. Our results imply that the forcing by surface temperature alone only weakly impacts on the spatial development of precipitating convective cells or the intensity of precipitation in the course of this development. Cold pools have often been implicated in the organization of the cloud field [*Böing et al.*, 2012; *Schlemmer and Hohenegger*, 2014], and cold pools may mediate horizontal "communication" between convective clouds. The lateral speed of cold pools may be dependent on the strength of the precipitation event causing them [*Feng et al.*, 2015], as the stronger evaporative cooling would then strengthen the density gradient between the cold pool and the adjacent environment as well as the effective height of the cold pool. Larger rates of scale increase could hence potentially be induced by faster cold pool spreading [*Linden*, 2012]. With some observational studies suggesting that cold pools might, in fact, be strong compared to those in some

models [*Engerer et al.*, 2008], a more direct comparison of high-resolution simulations with corresponding observations is urgently needed.

Notwithstanding the greater complexity of real-world precipitation extremes through wind shear, large-scale lifting or large-scale moisture advection, we speculate on the possible origin of temperature-related convective precipitation extremes [*Lenderink et al.*, 2009; *Berg et al.*, 2013; *Molnar et al.*, 2015]: the increases seen there might be attributable to typically earlier onset of precipitation within the day and subsequently more time for convective self-organization, which in turn leads to heavier extremes.

Climate models are pushing to resolve finer and finer scales, and long-term simulations using so-called convection permitting models (CPMs) are becoming feasible. Such models typically operate at resolutions of kilometers and can capture some aspects of larger convective cloud systems. Large-eddy simulations, as we use them here, have the advantage of being capable of resolving the spatial scale inherent to Rayleigh-Bénard convection (approximately kilometers) and can thereby address how this scale changes when precipitation forms. Our results therefore speak to dynamical organization that results from the very small scales and impacts on larger scales, possibly even influencing the organization found within CPMs.

LES model shortcomings may stem from cloud microphysical parameterization, resulting in quantitative uncertainty regarding the evaporation of precipitation and thereby the detailed cold pool properties. Overall, we advocate further research into universal, or overarching, features of convective cloud and precipitation evolution, guiding better understanding of convective self-organization and extremes. Such understanding may ultimately help implement parameterizations of small-scale convective structures in global climate models.

Acknowledgments
The authors acknowledge the German Weather Service, Meteorological Observatory Lindenberg, and F. Beyrich, for providing the Lindenberg observational data, as well as the University of Wyoming for the sounding data. C.M. acknowledges financial support from the project DH(CP)^2, funded by the German Federal Ministry of Education and Research. J.O.H. acknowledges support by a research grant (13168) from VILLUM FONDEN.

References

Agee, E., T. Chen, and K. Dowell (1973), A review of mesoscale cellular convection, *Bull. Am. Meteorol. Soc.*, *54*(10), 1004–1012.
Atkinson, B., and J. W. Zhang (1996), Mesoscale shallow convection in the atmosphere, *Rev. Geophys.*, *34*(4), 403–431.
Bénard, H. (1901), *Les Tourbillons Cellulaires Dans une Nappe Liquide Propageant de la Chaleur par Convection: En Régime Permanent*. Gauthier-Villars, France.
Berg, P., C. Moseley, and J. O. Haerter (2013), Strong increase in convective precipitation in response to higher temperatures, *Nat. Geosci.*, *6*(3), 181–185.
Böing, S. J., H. J. Jonker, A. P. Siebesma, and W. W. Grabowski (2012), Influence of the subcloud layer on the development of a deep convective ensemble, *J. Atmos. Sci.*, *69*(9), 2682–2698.
Emanuel, K. A. (1994), *Atmospheric Convection*, Oxford Univ. Press on Demand, Cambridge, U. K.
Engerer, N. A., D. J. Stensrud, and M. C. Coniglio (2008), Surface characteristics of observed cold pools, *Mon. Weather Rev.*, *136*(12), 4839–4849.
Feingold, G., I. Koren, H. Wang, H. Xue, and W. A. Brewer (2010), Precipitation-generated oscillations in open cellular cloud fields., *Nature*, *466*(7308), 849–852, doi:10.1038/nature09314.
Feng, Z., S. Hagos, A. K. Rowe, C. D. Burleyson, M. N. Martini, and S. P. Szoeke (2015), Mechanisms of convective cloud organization by cold pools over tropical warm ocean during the AMIE/DYNAMO field campaign, *J. Adv. Model. Earth Syst.*, *7*, 357–381, doi:10.1002/2014MS000384.
Koren, I., and G. Feingold (2011), Aerosol-cloud-precipitation system as a predator-prey problem, *Proc. Natl. Acad. Sci. U.S.A.*, *108*(30), 12,227–12,232, doi:10.1073/pnas.1101777108.
Lenderink, G., and E. van Meijgaard (2008), Increase in hourly precipitation extremes beyond expectations from temperature changes, *Nat. Geosci.*, *1*, 511–514.
Lenderink, G., E. van Meijgaard, and F. Selten (2009), Intense coastal rainfall in the Netherlands in response to high sea surface temperatures: Analysis of the event of August 2006 from the perspective of a changing climate, *Clim. Dyn.*, *32*, 19–33.
Linden, P. (2012), Gravity currents: Theory and laboratory experiments, in *Buoyancy-Driven Flows*, edited by E. Chassignet, C. Cenedese, and J. Verron, pp. 13–51, Cambridge Univ. Press, Cambridge, U. K.
Molnar, P., S. Fatichi, L. Gaál, J. Szolgay, and P. Burlando (2015), Storm type effects on super Clausius–Clapeyron scaling of intense rainstorm properties with air temperature, *Hydrol. Earth Syst. Sci.*, *19*(4), 1753–1766.
Moncrieff, M. W. (2010), The multiscale organization of moist convection and the intersection of weather and climate, in *Climate Dynamics: Why Does Climate Vary?*, edited by D.-Z. Sun and F. Bryan, pp. 3–26, AGU, Washington, D. C.
Moseley, C., P. Berg, and J. O. Haerter (2013), Probing the precipitation life cycle by iterative rain cell tracking, *J. Geophys. Res. Atmos.*, *118*, 13,361–13,370, doi:10.1002/2013JD020868.
Moseley, C., C. Hohenegger, P. Berg, and J. Haerter (2016), Convective extremes driven by cloud-cloud interaction, *Nat. Geosci.*, *9*, 748–752.
Neelin, J., O. Peters, J. W.-B. Lin, K. Hales, and C. Holloway (2008), Rethinking convective quasi-equilibrium: Observational constraints for stochastic convective schemes in climate models, *Philos. Trans. R. Soc. A*, *366*, 2581–2604.
Pincus, R., and B. Stevens (2009), Monte Carlo spectral integration: A consistent approximation for radiative transfer in large eddy simulations, *J. Adv. Model. Earth Syst.*, *1*, 1, doi:10.3894/JAMES.2009.1.1.
Rayleigh, J. (1916), On convection currents in a horizontal layer of fluid, when the higher temperature is on the under side, *Philos. Mag. Ser. 6*, *32*(192), 529–546.
Schlemmer, L., and C. Hohenegger (2014), The formation of wider and deeper clouds as a result of cold-pool dynamics, *J. Atmos. Sci.*, *71*, 2842–2858.
Schlemmer, L., and C. Hohenegger (2015), Modifications of the atmospheric moisture field as a result of cold-pool dynamics, *Q. J. R. Meteorol. Soc.*, *142*, 30–42, doi:10.1002/qj.2625.

Seifert, A., and K. Beheng (2006), A two-moment cloud microphysics parameterization for mixed-phase clouds. Part 1: Model description, *Meteorol. Atmos. Phys.*, *92*(1–2), 45–66.

Smagorinsky, J. (1963), General circulation experiments with the primitive equations: I. The basic experiment, *Mon. Weather Rev.*, *91*(3), 99–164.

Stevens, B., et al. (2005), Evaluation of large-eddy simulations via observations of nocturnal marine stratocumulus, *Mon. Weather Rev.*, *133*(6), 1443–1462.

Tompkins, A. M. (2001), Organization of tropical convection in low vertical wind shears: The role of cold pools, *J. Atmos. Sci.*, *58*(13), 1650–1672.

Torri, G., Z. Kuang, and Y. Tian (2015), Mechanisms for convection triggering by cold pools, *Geophys. Res. Lett.*, *42*, 1943–1950, doi:10.1002/2015GL063227.